Understanding photoluminescence in semiconductor Bragg-reflection waveguides

OPEN ACCESS
IOP Publishing
Journal of Optics
J. Opt. **23** (2021) 035801 (10pp)
https://doi.org/10.1088/2040-8986/abd888

Understanding photoluminescence in semiconductor Bragg-reflection waveguides

S Auchter[1,2], A Schlager[1], H Thiel[1], K Laiho[3], B Pressl[1], H Suchomel[4], M Kamp[4], S Höfling[4,5], C Schneider[4,6] and G Weihs[1]

[1] Institut für Experimentalphysik, Universität Innsbruck, Technikerstraße 25, 6020 Innsbruck, Austria
[2] Infineon Technologies Austria AG, Siemensstraße 2, 9500 Villach, Austria
[3] Institute of Quantum Technologies, German Aerospace Center (DLR), Söflinger Straβe 100, 89077 Ulm, Germany
[4] Technische Physik, Universität Würzburg, Am Hubland 97074 Würzburg, Germany
[5] School of Physics & Astronomy, University of St Andrews, St Andrews KY16 9SS, United Kingdom
[6] Institute of Physics, University of Oldenburg, D-26129 Oldenburg, Germany

E-mail: alexander.schlager@uibk.ac.at

Received 25 September 2020, revised 20 November 2020
Accepted for publication 5 January 2021
Published 18 February 2021

Abstract

Compared to traditional non-linear optical crystals, like BaB_2O_4, $KTiOPO_4$ or $LiNbO_3$, semiconductor integrated sources of photon pairs may operate at pump wavelengths much closer to the bandgap of the materials. This is also the case for Bragg-reflection waveguides (BRWs) targeting parametric down-conversion (PDC) to the telecom C-band. The large non-linear coefficient of the AlGaAs alloy and the strong confinement of the light enable extremely bright integrated photon pair sources. However, under certain circumstances, a significant amount of detrimental broadband photoluminescence has been observed in BRWs. We show that this is mainly a result of linear absorption near the core and subsequent radiative recombination of electron–hole pairs at deep impurity levels in the semiconductor. For PDC with BRWs, we conclude that devices operating near the long wavelength end of the S-band or the short C-band require temporal filtering shorter than 1 ns. We predict that shifting the operating wavelengths to the L-band reduces the amount of photoluminescence by 70% and making small adjustments in the material composition results in its total reduction of 90%. Such measures enable us to increase the average pump power and/or the repetition rate, which makes integrated photon pair sources with on-chip multi-gigahertz pair rates feasible for future devices.

Keywords: photoluminescence, semiconductor impurities, parametric down-conversion, Bragg-reflection waveguide

(Some figures may appear in colour only in the online journal)

1. Introduction

Entangled photons form the basis of many quantum applications, notably in computing and communication [1–4]. For this purpose, one would like to have sources that produce single photons, photon pairs or entangled photons at high rates with high quality. In practical realizations, various technological challenges arise which affect the efficiency or quality of the prepared photon states. This can

range from the simple dark noise in a detector to complex, parasitic non-linear optical interactions in an optical component.

While some strategies to handle and mitigate detrimental effects are often internal lab-knowledge (e.g. the ubiquitous black masking tape at the right places to shield detectors from background light), others are well-known techniques and approaches in the experiment or data post-processing. For example, in both bulk and integrated experiments, pulsed operation, time gating, and spectral and spatial filtering are commonly employed [5–9].

To be more specific, many quantum optics experiments are plagued by uncorrelated background light that produces spurious events and reduces the quality of the photon state and the signal-to-noise ratio [10]. This is not necessarily limited to the photon pair sources: In quantum cryptography applications, for example, light leakage can lead to compromised link security [11].

Integrated semiconductor quantum light sources are particularly susceptible to the parasitic influence of background light. Once the photonic chips have been fabricated, there are only limited options to include additional filters afterwards. Moreover, the presence of imperfections in semiconductor materials causes many complex light-matter interactions that are difficult to track down or get rid of.

Nevertheless, integrated photonic circuits have the advantage of overall stability and compact dimensions. Small dimensions lead to high field strengths which increase non-linear interactions. The further integration of light sources drastically improves the wall-plug efficiency of these chips, compared to bulk setups. This is all beneficial for many potential practical applications [1, 12], but especially for satellite technology [13, 14]. Thus, it is worthwhile to look at measures to suppress the parasitic effects already at the source level on the chip.

One example of integrated quantum light sources are Bragg-reflection waveguides (BRWs) that produce photon pairs via parametric down-conversion (PDC) [15–17]. They are made of multiple epitaxial layers of different alloys of aluminum gallium arsenide (AlGaAs). This material system possesses a large second-order optical non-linearity [18] and is versatile for designing and fabricating samples with the help of well-established techniques. A great benefit of AlGaAs is its potential to seamlessly integrate electro-optic elements, like light sources and modulators, with PDC on chip. The waveguides can be designed to operate at almost any temperature where the material is stable. While the technology still is not as mature as silicon or lithium niobate in certain aspects, most notably linear loss and homogeneity, it is improving quickly [19–21].

Recently, BRWs have become increasingly popular for PDC [17, 22–24], and considerable effort was dedicated toward optimizing their performance for different tasks. For example, not only integrated electrically injected pump lasers on the same chip as the PDC sources could be demonstrated [25, 26], but also various aspects of the preparation of polarization entangled states [27–29], like the compensation of the birefringent group delay [30].

In this paper, we conduct a series of experiments to determine the driving factors that affect the generation of photoluminescence in our BRWs, such as wavelength and power dependencies as well as the spatial field distribution. Photoluminescence in BRW structures similar to the ones investigated here has been reported by other groups [25, 28] as well, but was never studied in-depth. It was informally hypothesized that the impurities in the substrate are driving factors of the photoluminescence.

We note that such luminescence is not exclusive to PDC in semiconductors, but also exists in commonly employed crystals, like BaB_2O_4 or $KTiOPO_4$, especially when pumped with high-energy light [31–33]. At similar wavelengths to our BRWs, fluorescence is observed in periodically poled silica fibers [34] and spontaneous Raman scattering in four-wave-mixing schemes (FWM) [35]. In integrated quantum optics, parasitic background light has also been observed in p-i-n diode based single-photon sources [36] and quantum-dot based systems [37].

1.1. Aspects of photoluminescence in integrated PDC sources

The challenge of parasitic photoluminescence in integrated PDC sources of photon pairs is that they operate in the linear low-gain regime [38]. In contrast to classical second-harmonic generation, difference frequency generation or optical parametric oscillation schemes, the efficiency *does not* increase with increasing pump power. Typical PDC signal rates are in the kHz to GHz range which are many orders of magnitude smaller than the photon rate of the pump light ($\gg$PHz). These drastically different amounts of optical power in the device mean that even very inefficient photoluminescence processes can easily produce photons at rates similar to those of the PDC.

The observed photoluminescence rates depend on the power non-linearity of the underlying process: If the PDC is pumped with a pulsed laser incorporating a high peak power, non-linear photoluminescence generation is either greatly enhanced or somewhat suppressed, compared to the continuous wave (CW) case. The former corresponds to unrestricted two- or multi-photon absorption, while the latter indicates saturation.

PDC in BRWs is based on the interaction between the fundamental and higher-order spatial modes. One challenging aspect in this regard is that BRWs do not operate in a single-mode regime, but support higher-order modes with different mode profiles. These characteristic profiles are the result of the stratified layout made from different material compositions and the horizontal confinement of the ridge. Hence, the layers are exposed to different amounts of light depending on whether we look at the pump or PDC wavelength. For example, the pump mode is localized in the central core layer, while the fundamental telecom mode of the PDC photons mostly propagates in the two layers right adjacent to the core. Of course, the material composition of these is different from the core, which results in additional complications when analyzing the inter-play of pump light, PDC and the photoluminescence.

Due to the complicated modal structure, it is easy to excite many spatial modes simultaneously, not always intentionally. Therefore, a considerable amount of light can excite the semiconductor material, but will not partake in down-conversion [19]. There are also many modes which not only excite the impurities, but will guide any photoluminescence along the ridge. These conditions are sub-optimal as the PDC also propagates in the waveguide. Various external improvements have been proposed to reduce the effective multi-modeness, for example beam-shaping via holographic elements or integrating the pump laser [25, 26]. Narrow temporal filtering below 3 ns is commonly employed, and we have previously shown that additional spectral filtering is highly effective [22].

In this work, however, we *intentionally ignore* these *best practices* in order to get a clear photoluminescence signal. Aside from this, we keep the experimental methodology as close to normal operation as possible to get an idea how the photoluminescence affects the expected use case. We use an excitation laser with a Gaussian beam profile and use only wide time-gates of 13 ns (=pulse repetition time of the laser). This allows us to model the photoluminescence from studying the single and coincidence rates with varying frequency and incident power. One goal is to separate the contribution of the photoluminescence from the PDC. In this context, we also study whether the specific design of the sample can be improved to reduce noise.

The data presented here reveals that the photoluminescence results from linear absorption at the bandgap of one or more layers near the core of the waveguide. Once an electron–hole pair is excited, the radiative recombination takes place at impurities at half the bandgap energy. Photoluminescence from these deep levels can be related to lattice defects, like antisites (arsenic) or vacancies, or certain rare dopants [39]. Moreover, we operate our device at room-temperature, therefore a rather broad, quasi-uniform photoluminescence spectrum is expected [39]. This is consistent to measurements in previous experiments [40].

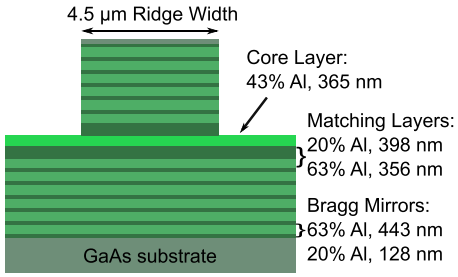

Figure 1. Schematic illustration of the BRW sample. Our BRWs are monolithically grown on a GaAs substrate via molecular beam epitaxy, the ridges are patterned by electron beam lithography and dry etched to just above the core in Argon and Chlorine plasma. The matching layers underneath and on top of the core layer enhance the modal phasematching of the contributing Bragg-mode and total-internal-reflection modes, corresponding to the spatial modes in the pump and PDC wavelengths, respectively. Around them are six alternating layers of $Al_{0.63}Ga_{0.37}As$ and $Al_{0.20}Ga_{0.80}As$ that form Bragg mirrors in order to confine the light in the transverse vertical direction.

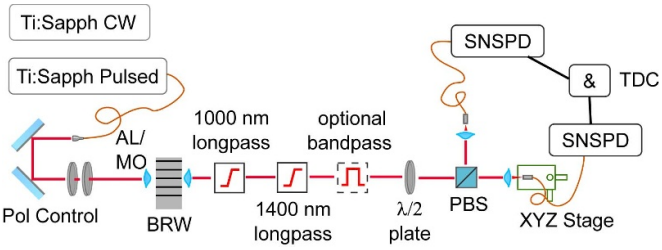

Figure 2. Sketch of the main setup for the pulsed excitation. The selected pump laser is coupled into the waveguide via an aspheric lens (AL) or a microscope objective (MO) on one side and the generated PDC is collected with another AL at the output facet. After collimation, the pump is suppressed by two longpass filters, followed by an optional bandpass. The photon pair is split deterministically at the polarizing beam splitter (PBS) and coupled to fibers via ALs on the XYZ translation stages and detected and correlated subsequently.

2. Methods

2.1. Sample and setup

The BRW sample under investigation depicted in figure 1 is a state-of-the-art, low-loss, matching-layer enhanced design optimized for simple fabrication, while simultaneously allowing a bright type-II PDC process [21, 41]. Our experimental setup is shown in figure 2. For illumination, we switch between two different pump lasers. The first is a Coherent MIRA titanium sapphire laser running in femtosecond mode, with the pulses being stretched to 1.5 ps by a pulse stretcher. The pulse repetition rate is 76.2 MHz, which corresponds to a 13.1 ns delay between pulses. The second is a CW Tekhnoscan T&D-scan X1 titanium sapphire laser. The selected pump laser is coupled into the waveguides via an aspheric lens (AL) or a microscope objective (MO) on one side, the generated PDC is collimated with another AL at the output facet. Two longpass dichroic interference filters remove the residual pump beam. An optional 40 or 12 nm bandpass filter, nominally centered at 1550 nm, follows before the photon pairs are split by a polarizing beam splitter (PBS). The central wavelength of the bandpass is slightly tunable by rotating the filter a few degrees with respect to the beam. After the PBS, we couple the photons via collimation optics into single mode fibers connected to high-efficiency SingleQuantum EOS superconducting nanowire single photon detectors (SNSPDs). The output of the SNSPDs is amplified, routed to threshold discriminators and detected by a quTools quTau time-to-digital converter. All optics have the necessary broadband coating and suitable glass. This ensures a reflectivity of less than 1% at a 100 nm away from the nominal operating wavelengths.

We conduct three experiments: The first in section 3.1 serves as a sanity check, testing the spatial distribution of the PDC and photoluminescence signals at the facet. Here, we move the collection fiber (single-mode) parallel to the facet to verify that both signals are indeed coming from the waveguide. The second experiment in section 3.2 yields a precise model of the PDC and noise. We vary the pump power and employ various bandpass filters after the waveguide while recording

the channel rates and coincidences. The final experiment in section 3.3 reveals more about the cause of the photoluminescence by measuring the signal power at pump wavelength strongly detuned from the degeneracy point.

For convenience, we operate two almost identical setups according to figure 2. In sections 3.1 and 3.3 we employ a waveguide with a length of 2.04 mm and a degeneracy wavelength of 767 nm as well as a MO for the in-coupling. In sections 3.2 and 3.4 a 1.3 mm long waveguide with 763 nm degeneracy wavelength is utilized and an AL is employed for in-coupling. To ensure comparability, both are from the same wafer. These wavelengths are shorter than the design wavelength of 775 nm. Depending on the location of the chip on the wafer and the waveguide width some variability was observed. We intentionally choose waveguides with shorter operating wavelengths, as they are closer to the bandgap of the material and yield a clearer combined PDC-photoluminescence signal as investigated in section 3.3.

The main experimental challenge is keeping all light sources and the setup stable under comparable and reproducible conditions. This imposes a practical limit how much usable data we can actually acquire in a certain time-frame. As some components, like filters, need to be changed for every set, the coupling varies and quick re-alignment is necessary. Therefore, we optimize the setup on metrics that can be derived in real-time in the lab[7], most importantly the raw coincidence count rate. We operate the setup in a tightly controlled environment suitable for precision interferometry as reported in our [43].

2.2. Rate models for the PDC and photoluminescence

For analysis, we model the observed rates on the detectors ('singles') as well as the coincidences rates to simultaneously estimate the intrinsic PDC pair production rate and photoluminescence. This approach has been applied to various processes, such as PDC [44, 45] or FWM [46, 47]. In our case, the model is the system of equations,

$$R_s = \eta_s \left(\xi P + f(P)\right) + R_{\mathrm{bg}}, \tag{1}$$

$$R_i = \eta_i \left(\xi P + f(P)\right) + R_{\mathrm{bg}} \text{ and} \tag{2}$$

$$R_c = \eta_s \eta_i \xi P + \tau_c R_s R_i, \tag{3}$$

which we solve for the detected coincidence rate R_c. Empirically, we know that the background rate R_{bg} is equal for both channels, which we include directly in the model[8]. The single count rates in equations (1) and (2) are eliminated, allowing us to write R_c in terms of the incident optical power P, the efficiency to generate photon pairs from that power ξ, the heralding efficiencies of 'signal' and 'idler' η_s and η_i according to the Klyshko scheme [48], and the coincidence window τ_c. Similar to the intra-waveguide PDC generation rate ξP, the noise model $f(P)$ describes the amount of photoluminescence generated depending on pump power.

A power law is the simplest noise function, which is given by

$$f(P) = \gamma_P P^{\alpha}, \tag{4}$$

with γ_P being the photoluminescence generation efficiency, equivalent to ξ. This model is easy to interpret via the exponent α in terms of the number of photons that are involved. If it is dominated by two- or multi-photon processes or exponential avalanche effects, like in laser resonators, the exponent α is greater or equal than 2. A value of 1 corresponds to linear absorption, smaller than 1 indicates saturation.

The second proposed noise function describes a saturable absorber, we assume a 'dead-time' model [49] given by

$$f(P) = \frac{\gamma_S P}{1 + \beta \gamma_S P}. \tag{5}$$

Here, β corresponds to an effective lifetime (or dead-time) of an ensemble of light emitting defects and γ_S corresponds to γ_P in equation (4). We focus only on these two noise models as others, like ones based on error functions $\propto \mathrm{erf}(P)$ or exponentials $\propto 1 - \exp(P)$ fail to converge satisfactorily over the whole power range for the data presented in section 3.2.

3. Results

3.1. Spatial distribution of the photons at the facet

For start, we determine the spatial distribution of the PDC and background counts of the 2.04 mm waveguide. This is done to verify that both coincidences and background originate at the waveguide and are not collected from somewhere else. Moreover, there have been previous hypotheses that the background results from impurities in the GaAs substrate [25], which can be verified by comparison with the spatial distribution of the PDC signal.

The collection fiber is held by a clamp mounted on an Elliot Scientific MDE510 fiber launch system. The fiber can be moved in X, Y, and Z-directions relative to the fixed collimating lens. We measure the distribution by moving the fiber in the imaging plane parallel to the waveguide facet. Due to the different focal lengths of the collimating lenses, the image of the waveguide facet is magnified 5.8 times at the plane of the collection fiber.

This approach is limited in resolution by the collection spot size and the difficulty to determine the absolute position of

[7] With a more time-consuming and elaborate optimization procedure, values similar to better than the ones reported in [22] can readily be achieved (e.g. [42]).

[8] In principle, as the channels are separated by polarization in the setup in figure 2, polarized background light split at the PBS and coupled to the fibers could cause an imbalance. However, we have not observed such an effect in our system. In fact, the SNSPD bias current is set to a value that a mean dark-rate of 300 s^{-1} is achieved. Thus, the quantum efficiency might be slightly different for different detectors. This is taken care of by measuring the heralding efficiencies.

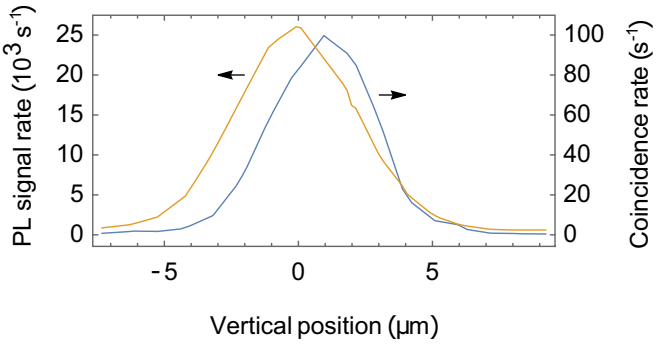

Figure 3. Vertical slice of the photoluminescence signal (orange, left scale) and the coincidences of the PDC (blue, right scale). The peak of the background is slightly below the peak of the PDC coincidences.

the spot on the facet. The latter can be partially circumvented, as we optimize the coupling for maximum coincidences. According to simulations, the maximum of the coincidences is the center of the ridge and the center of the core layer. We choose this easy to find position as our reference point. First, we scan the distribution of the coincidences, starting with the maximum. Then, we optimize for maximum coincidences again and change the wavelength of the pump lasers, so that no PDC can be detected. This allows us to repeat the same measurement for the photoluminescence using the same reference frame.

In the horizontal direction, which is parallel to the epitaxial layers, both distributions are perfectly centered, but the photoluminescence is much wider. In vertical direction, which is perpendicular to the layers of the BRW structure, the photoluminescence is also wider and the maximum is shifted by approximately 1 μm toward the substrate, as shown in figure 3. We observe little to no light from the substrate, even though the peak of the photoluminescence is observed slightly shifted toward the substrate. A possible explanation for the wider and shifted emission of the photoluminescence is that there are many modes the impurities can emit into, instead of just the total internal reflection modes for PDC. They may even be only weakly guided and just diffract through the sample, but only the parts that are actually collected are relevant in further experiments.

The GaAs substrate is semi-insulating, which increases the total number of impurities and potentially the photoluminescence. In contrast to previous hypotheses about the spatial distribution [25], our data suggests that the substrate causes little or no relevant photoluminescence. This is important for electrically active samples: If a heavily doped substrate is required to contact the waveguide from below, it will not affect the noise generation rate. Nevertheless, higher doping in the core regions increase the number of impurities, so more photoluminescence has to be expected.

3.2. Rate models from power sweeps at the degeneracy wavelength

In the second experiment, we record the single count rates as well as the coincidences in a 13 ns time window over three orders of magnitude of input power and compare them with the case of narrower temporal time-gating of 1.13 ns. The power sweeps are carried out at a pump wavelength of 763 nm, which is approximately 0.3 nm below the degeneracy wavelength of the employed 1.3 mm long waveguide. This wavelength was chosen empirically, as it is a stable and repeatable laser operating point. We select average pump powers with logarithmic spacing between 10 and 1000 μW, the typical operating range of our waveguides when pumped externally.

Each power sweep corresponds to one of four conditions: (1) Pulsed pump without filter, (2) pulsed pump with 40 nm or (3) pulsed pump with 12 nm bandpass filter. The bandpass filters are centered at the degeneracy wavelength of the produced signal and idler photons. For condition (4), we remove the bandpass and couple a CW laser into the waveguide. The rationale behind this approach is two-fold: First, the SNSPDs are able to detect light well outside the telecom C-band, we can therefore test the effectiveness of bandpass filtering under pulsed pump conditions. We know from previous measurements that the spectrum of the photoluminescence is very broad and uniform, and that spectral filtering is effective in increasing the signal-to-noise ratio [40]. Second, the peak power in the pulsed case is roughly 10^6 times higher than in the CW case for the same average power. Any non-linear effects, like two-photon absorption, should therefore be clearly discernible.

The coefficients of two PDC models with different noise functions are given in table 1, the raw data with power-law fits and with the saturation models are depicted in figure 4. For comparison, the analysis with a narrower time gate of 1.13 ns is shown in figure 5. Here, only the rate model for the PDC without photoluminescence is fitted. Looking at the data for CW, we suspect that the data point at 20 μW is an outlier and is subsequently excluded. Note, that the 12 nm bandpass filter cut way too much signal to get enough data for a sound analysis.

We then take a closer look at the estimated PDC pair generation rates ξ. As the setup and waveguide remain identical in between experiments, these values speak for the consistency of our measurements. Most of the rates are within the range of 5×10^5 pairs μW^{-1}s^{-1} to 8×10^5 pairs μW^{-1}s^{-1} without filters, and an order of magnitude less with a 40 nm bandpass filter. The only exception is the saturation model in the *No filter (CW)* case, which reports pair rates more than twice as high as the other cases. The parameter values quoted here represent a 'majority consensus' of the saturation model: It may seem obvious at first to mark the measurement at 20 μW as outlier, but selectively removing each data point paints a different picture. In fact, removing the *first* (10 μW) point, results in parameter values much closer to the other fits ($\xi = 0.5(2) \times 10^6$ pairs s^{-1} μW^{-1}, $\gamma_P = 2.4(2) \times 10^6$ photons s^{-1} μW^{-1}, $\beta = 0.6(2)$ ns, p-value < 0.05). This does not happen with the power law model, which seems to be more stable in general. In that sense, the values from table 1 should be seen as defining the bounds of what parameter range to expect.

However, this analysis also raises the question of whether a reduction to a tenth of the PDC rate is agreeable when employing 40 nm bandpass filter. As the spectrum of the PDC is

Table 1. Fit coefficients of the two noise models for different pump/filter conditions according to equations (1)–(3). The data measured with the 40 nm bandpass filter can be well explained without a noise model. Most quoted parameter values exhibit a p-value of lower than 0.01, except for ξ in the *No filter (CW) power law* case and β for *No filter (pulsed), saturation model* (both $p = 0.1$). The R^2 is always better than 0.95. The coincidence window is 13.1 ns (= 1/laser repetition rate), except where stated.

PL model	Parameter	No filter (pulsed)	40 nm BPF (pulsed)	No filter (CW)
Power law equation (4)	ξ (10^6 pairs $s^{-1}\mu W^{-1}$)	0.5(1)	0.060(1)	0.5(2)
Noise $\propto \gamma_P P^\alpha$	γ_P (10^6 photons $s^{-1}\mu W^{-1}$)	2.0(4)	n/a	8.5(5)
	α	0.74(4)	n/a	0.70(3)
Saturation equation (5)	ξ (10^6 pairs $s^{-1}\mu W^{-1}$)	0.78(6)	0.060(1)	1.40(6)
Noise $\propto \gamma_S P/(1+\beta\gamma_S P)$	γ_S (10^6 photons $s^{-1}\mu W^{-1}$)	0.4(1)	n/a	2.5(2)
	β (ns)	8(6)	n/a	5(1)
Short time gate (1.13 ns)	ξ (10^6 pairs $s^{-1}\mu W^{-1}$)	0.80(1)	0.062(1)	1.80(3)
Klyshko efficiencies	$\eta_s \times 10^{-4}$	1.9(1)	4.9(2)	2.6(1)
	$\eta_i \times 10^{-4}$	1.5(1)	8.5(3)	3.2(1)

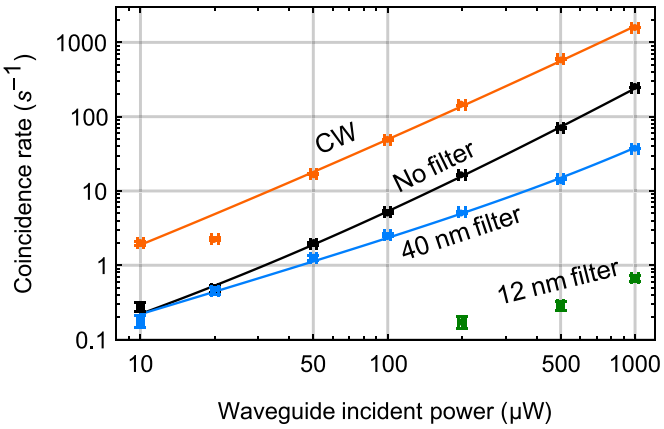

Figure 4. Recorded coincidences with a fit representing the power law and the saturation model for the photoluminescence using a 13 ns window. The two models produce almost identical curves in the displayed range.

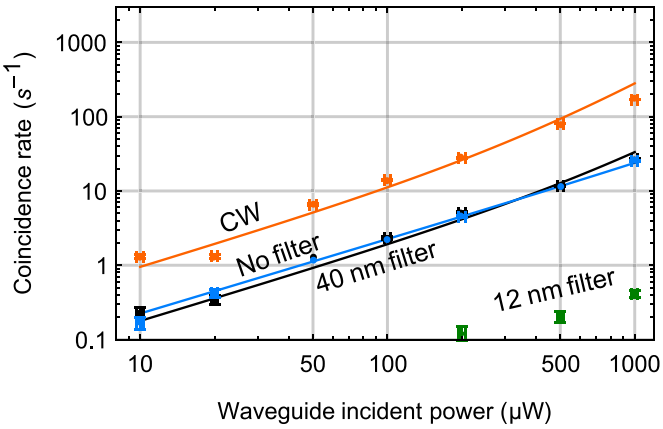

Figure 5. Recorded coincidences using a narrow 1.13 ns window. Here, photoluminescence models are not needed ($f(P) = 0$) to explain the curves statistically well enough.

more than 90 nm FWHM wide [22], a considerable reduction in power can already be expected. Including the transmission profile of the filter, we determine that only approximately 32% of the signal/idler photons are transmitted, while the rest is absorbed or reflected by the filter. As coincidence rates are affected twice, due to the involvement of two correlated photons, the total PDC transmission is expected to be about 10%, which is consistent with our results for the PDC rates.

Moreover, as the noise is spectrally broader than the PDC [40], the signal-to-noise ratio increases. This is evident as the model without photoluminescence (γ_S or $\gamma_P = 0$) yields a statistically significant fit in table 1.

Our results show that the exponents of the photoluminescence power law model are significantly below 1. This indicates that the driving factor of the photoluminescence is saturable linear absorption, and that higher-order photon processes play only marginal roles in our experimental conditions. In the following section 3.3, the dependence of the photoluminescence generation rates on the pump wavelength supports this hypothesis. The saturation is modeled as an excitation with a lifetime, which assumes that the photoluminescence stems from impurities that can only be re-excited after a delay when emitting a photon.

We emphasize that the photoluminescence scale factors γ_S and γ_P serve the same purpose, but their values cannot be compared directly without taking $f(P)$ into account. The true rate is only given by $f(P)$. For example, at high powers $f(P)$ predicts a much higher photoluminescence rate for the saturation model compared to the power model. At low powers it is vice-versa. Both models can explain the overall shape of the curves well and statistically sound. Further discussions about the differences are given in section 3.4 and figure 8.

Note, that the Klyshko efficiencies are two orders of magnitude lower as in our previous work, which is caused by the nature of this experiment. As we are deliberately trying to measure the photoluminescence, we refrain from tight spatial, temporal or spectral filtering. Hence, the single rates increase by a large amount, while the coincidence rates stay relatively low. In our previous work [22], we report up to $\eta \sim 6\%$ by employing the proper filters.

3.3. Off-resonant photoluminescence generation rates

In the final experiment, we move the excitation wavelength away from the degeneracy point, mostly toward longer wavelengths where no PDC is produced, because the phasematching condition is no longer fulfilled. On occasion, we have observed PDC processes of various types that probably involve higher-order modes in several waveguides. We avoid these wavelengths in this experiment to focus solely on the photoluminescence. We measure the magnitude and linearity of the photoluminescence at each wavelength for different excitation powers.

In this section, we employ the setup with the MO and the sample with a length of 2.04 mm (degeneracy wavelength 767 nm). We use a 40 nm bandpass filter and a pulsed pump to emulate the conditions for a typical broadband PDC experiment with BRWs.

Without the PDC, we neglect coincidences so the full rate model is no longer necessary. Instead, we simply record the rates on one of the SNSPDs, measuring only dark counts plus the photoluminescence. This can be described by a power law with an offset

$$R_s(P) = AP^{\alpha} + R_0, \tag{6}$$

where P is the power before the waveguide in-coupling objective. The scale factor of the polynomial A can be interpreted as the photoluminescence generation rate, R_0 is the count rate at the lowest power measured, including dark-counts and background. The exponent α corresponds to the one from the fits and models discussed in the previous section 3.2, but is determined independently for each photoluminescence data set. This model shows an excellent agreement with the measured data in figure 6. The resulting fit coefficients are listed in table 2. We find that α is very close to one, with the tendency that shorter wavelengths slightly deviate toward lower exponents. This is a further hint at saturation effects, which are more noticeable the closer the excitation wavelength is to the bandgap of the materials. We note that the value of the exponent can only be compared qualitatively between samples. The exact nature, realisation and excitation of the impurities can vary between the waveguides, resulting in slightly different rates and exponents.

The photoluminescence generation rate A (table 2) shows a distinct behavior in figure 7. Over the span of 100 nm above the bandgap, it decreases by two orders of magnitude. To model this behavior, we tried a variety of functions, like polynomials or exponentials similar to the overlap integrals known from solid state physics [50]. It turns out, the only viable model is a Lorentzian function given by

$$A(h\nu) = \frac{\mathcal{N}}{1 + \left(\frac{h\nu - E_g}{\sigma}\right)^2}. \tag{7}$$

While $\mathcal{N}$ and σ are just scale parameters, the position of the resonance, $E_g = 1.654(4)\text{eV} \approx 750\,\text{nm}$, can be explained physically: Its value is very close to the bandgap of the matching layers with an aluminum concentration of nominally 20%.

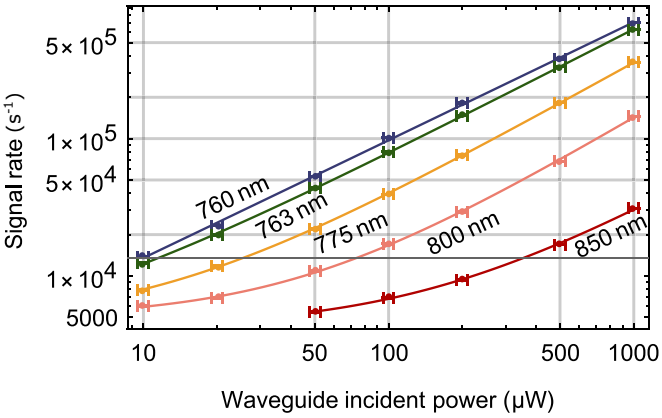

Figure 6. Raw data of the off-resonant photoluminescence generation rates at telecom wavelengths for different average excitation powers and pump wavelengths between 760 and 850 nm. The data is fitted with the power law from equation (6). The fit parameters are listed in table 2, the generation rate A is plotted in figure 7.

Table 2. Fit coefficients of the power law with offset from equation (6)

Wavelength (nm)	A (photons $\mu\text{W}^{-1}\text{s}^{-1}$)	α	R_0 (photons s^{-1})
760	1800(300)	0.86(3)	100(1400)
763	1130(150)	0.91(3)	3000(1000)
775	360(50)	1.00(2)	4400(400)
800	87(13)	1.07(3)	5000(140)
850	27(10)	1.00(6)	4200(300)

The Lorentzian function is an excellent approximation for the real and imaginary parts of the dielectric function near the bandgap of $Al_xGa_{1-x}As$ alloys with an aluminum concentration of x [51]. In the literature, the quoted bandgap of $Al_xGa_{1-x}As$ varies slightly [51–53]. If we also take the typical fabrication error of the concentration of about two percentage points into account, our estimation of E_g corresponds to an aluminum concentration of 18.5%–19.5%, which is well within the manufacturing specification. Together with the rate modeling from the previous section 3.2, this strongly indicates that linear absorption is indeed the driving factor of the photoluminescence.

3.4. Considerations for future devices

Identifying and modelling the driving factors of the photoluminescence allows us to improve future samples. The first and foremost measure is increasing the spread between the lowest bandgap and the design wavelength. We propose two measures to reduce the noise: longer operating wavelengths and lower bandgap materials.

Quantitatively, we can estimate the effect of these proposals for the sample at hand from the fit in figure 7. First, moving from a 767 to a 780 nm pump wavelength already reduces the amount of photoluminescence by 70%. Second, our powerful automated sample design suite [21] allows us to

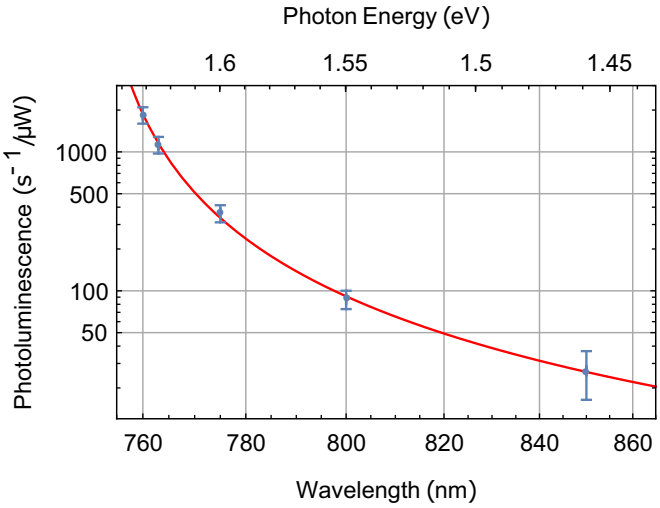

Figure 7. Noise generation rate A from table 2 with Lorentzian fit according to equation (7). The resonance is centered at 1.654(4) eV (750 nm), which is approximately the bandgap of the matching layer materials.

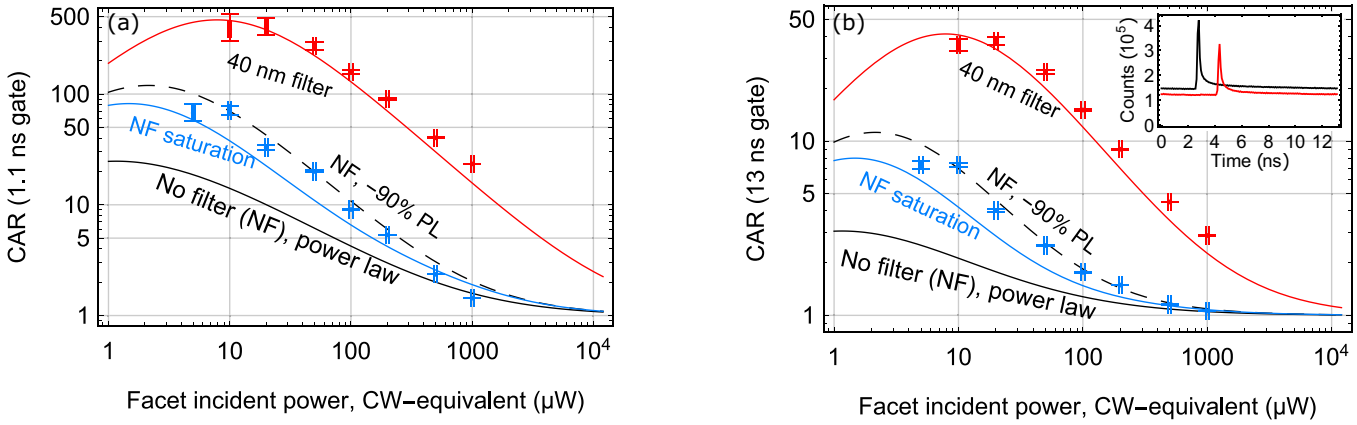

Figure 8. Predicted CAR values for different conditions with a pulsed pump at 76.2 MHz repetition rate. At low powers, the CAR is limited by the dark counts of the detectors (300 s^{-1}), at high powers by the accidental coincidences. Both the raw data (symbols) from figures 4 and 5 and curves derived from the different models (40 nm, red and No filter, black and blue) are shown. The black solid line depicts the no filter power law model, while the blue line is the corresponding saturation model, showing better agreement to the measurements, especially at low powers. The dashed line is a hypothetical sample, with the photoluminescence reduced by 90%. Here, choosing either the power law or saturation model made no significant difference. (a) shows the time filtered case with a 1.13 ns time gate, (b) the unfiltered with 13.1 ns. Note that the vertical scales are different by an order of magnitude. The inset in the upper right shows the time traces of the signal (red) and idler (black) emission when utilizing the pulsed laser at 1000 μW power with no filter. In comparison to the sharp peaks of the PDC signal, the photoluminescence appears as a very broad background—further emphasizing the benefit of short time gates.

easily modify the sample to increase the aluminum concentration. For example, changing just the two matching layers next to the core from a concentration of 20%–22%, reduces the photoluminescence by another 60%. Both measures increase the spread between excitation and bandgap edge and result in a 90% total reduction compared to the samples investigated here. It is important to note that these small changes do not affect the critical performance metrics [21] of the waveguide, like the mode overlap and the effective non-linearity.

Furthermore, since we now have the full rate model description (equations (1)–(3) and table 1) of our 1.3 mm long waveguide at hand, we calculate the coincidence-to-accidentals ratio (CAR) curves for different filters and potential alternative designs, which may have modified material compositions, other geometries or shifted design wavelengths. A great advantage of this model-based approach is the separation of the PDC and noise signal. This allows us to evaluate the effects of different coincidence windows on the figures of merit.

The results for two different coincidence windows are depicted in figure 8. It is clearly visible that spectral filtering and time filtering prove to be highly effective, as a model without photoluminescence can explain the measured data well. A narrow time gate increases the maximum CAR by a factor of 10. Without spectral filter, a noise-optimized design could increase the usable pump power substantially for a fixed CAR. The saturation model without spectral filters (solid blue line) in figure 8 yields a CAR of 7 at 100 μW pump power. Keeping the CAR constant and moving to the dashed line representing a sample with 90% reduction in the photoluminescence, shows a pump power of around 200 μW—which corresponds to doubling the pair rate.

Furthermore, it is clearly visible that both noise models have their merits. We believe the power law in equation (4) provides a good estimate of the PDC production rate, while the saturation model in equation (5) provides a good description of the processes at lower powers. The slight discrepancy with the measured data, however, also shows that we still cannot capture the full physics of our system. Moreover, the fact that two parameters in table 1 could only be fitted to a p-value of 0.1 indicates the limitations of the statistics and the models in certain cases. Building the model from a pure quantum optics approach, i.e. mean photon numbers, failed to produce reliable results over the whole power range.

We emphasize that the values reported in figure 8 are conservative in the sense that we did not explicitly align for maximum CAR. Properly optimizing the pumping and coupling, also in connection with narrower filtering (e.g. 12 nm bandpass), yields values at least an order of magnitude higher [42]. This can be seen instantly as the graph for 90% reduction is not even close to the 40 nm case, which it should be. With better alignment, however, there is much headroom for optimizing for the individual case. Nevertheless, it follows that for these hypothetical samples, the filtering requirements are relaxed significantly compared to the state-of-the-art. This can be especially interesting for any integrated detection system: Realizing high fidelity time filtering to the picosecond level is much harder than just to nanoseconds. This is also true for on-chip spectral bandpass filters.

Having the full model depending on the input power allows us not only to estimate the CAR, but also to predict pair rates for an on-chip pump and photonic network. As all the stated input powers are measured before the AL, we need to determine the individual loss factors for coupling into the waveguide. The actual power guided in the pump mode can be recovered by multiplying the AL transmission (70%) with the total in-coupling efficiency (<35%) and the typical relative pump mode excitation (>4%) [19]. Thus, only 1% of the power reaches the necessary pump mode. Hence, we estimate that the *true* coefficient of pair generation rate, e.g. for an on-chip pump, is in fact on the order of $5 \times 10^7\ \mu\mathrm{W}^{-1}\,\mathrm{s}^{-1}$. In a pure externally pumped system, this is not achievable due to absorption of the glass in the objective, even with proper beam shaping to match the far field mode shape. In contrast, an active, electrically pumped, waveguide laser runs intrinsically in the correct mode [25, 26]. This means that for 1 mW of internal laser power, a pair rate of at least 5 GHz can be expected. Such rates are tremendously useful as they can be harnessed by a fully integrated (quantum) optic network.

4. Conclusion

We have presented three different measurements designed to gain insight into the nature of BRW photoluminescence. We proposed two rate models to describe the photon generation process from a big-picture point of view. There is strong evidence that the main cause of photoluminescence is electron–hole pair excitation via linear absorption of a pump photon, followed by a short lived radiative decay via deep impurity levels. The defects that provide these deep levels are located in the matching layers with a low aluminum concentration right next to the core. Furthermore, we have proposed small modifications in the sample design that promise to greatly reduce the photoluminescence. Our calculations predict a reduction by 90%, while promising high non-linearity and photon pair rates in the GHz regime.

Author contributions

Conceptualization, S A, K L, B P, G W; Formal analysis, S A, B P; Methodology, S A, A S, K L, B P, G W; Investigation, S A, A S, K L, B P, H T; Resources, H S, M K, S H, C S; Software, B P; Supervision, B P, G W; Writing—original draft, S A, B P; Writing—review & editing, A S, K L, H T, C S, G W; Funding acquisition, C S, G W.

Acknowledgments

This work was supported by the Austrian Science Fund (FWF) through the project I2065 and the Special Research Program (SFB) project *BeyondC* no. F7114, the DFG Project No. SCHN1376/2-1, the ERC project *EnSeNa (Grant No. 257531)* and EU H2020 quantum flagship program *UNIQORN (Grant No. 820474)* and the State of Bavaria. S A is supported by the EU H2020 FET open project *PIEDMONS (Grant No. 801285)*. B P acknowledges support by the FWF SFB Project No. F6806. We thank A Wolf and S Kuhn for assistance during sample growth and fabrication. We thank T Günthner and H Chen for laboratory assistance and S Frick, M Sassermann, R Chapman and M Prilmüller for fruitful discussions and comments.

ORCID iDs

A Schlager https://orcid.org/0000-0002-3587-8847
K Laiho https://orcid.org/0000-0003-3090-8629
B Pressl https://orcid.org/0000-0001-9098-555X
S Höfling https://orcid.org/0000-0003-0034-4682
G Weihs https://orcid.org/0000-0003-2260-3008

References

[1] O'Brien J L 2007 *Science* **318** 1567
[2] Rudolph T 2017 *APL Photon.* **2** 030901
[3] Ma X-S *et al* 2012 *Nature* **489** 269
[4] Günthner K *et al* 2017 *Optica* **4** 611
[5] Aspect A, Grangier P and Roger G 1981 *Phys. Rev. Lett.* **47** 460
[6] Kwiat P G, Mattle K, Weinfurter H, Zeilinger A, Sergienko A V and Shih Y 1995 *Phys. Rev. Lett.* **75** 4337
[7] Patel K A, Dynes J F, Choi I, Sharpe A W, Dixon A R, Yuan Z L, Penty R V and Shields A J 2012 *Phys. Rev.* X **2** 041010
[8] Eraerds P, Walenta N, Legré M, Gisin, N and Zbinden H 2010 *New J. Phys.* **12** 063027
[9] Schweickert L *et al* 2018 *Appl. Phys. Lett.* **112** 093106
[10] Shields A J 2007 *Nat. Photon.* **1** 215

[11] Brassard G, Lütkenhaus N, Mor T and Sanders B C 2000 *Phys. Rev. Lett.* **85** 1330
[12] Politi A, Cryan M J, Rarity J G, Yu S and O'Brien J L 2008 *Science* **320** 646
[13] Armengol J M P *et al* 2008 *Acta Astronaut.* **63** 165
[14] Yin J *et al* 2017 *Science* **356** 1140
[15] Lanco L, Ducci S, Likforman J-P, Marcadet X, Van Houwelingen J, Zbinden H, Leo G and Berger V 2006 *Phys. Rev. Lett.* **97** 173901
[16] Sarrafi P, Zhu E Y, Dolgaleva K, Holmes B M, Hutchings D C, Aitchison J S and Qian L 2013 *Appl. Phys. Lett.* **103** 251115
[17] Horn R, Abolghasem P, Bijlani B J, Kang D, Helmy A S and Weihs G 2012 *Phys. Rev. Lett.* **108** 153605
[18] Boyd R W 2003 *Nonlinear Optics* (New York: Academic)
[19] Pressl B, Günthner T, Laiho K, Geßler J, Kamp M, Höfling S, Schneider C and Weihs G 2015 *Opt. Express* **23** 33608
[20] Porkolab G A, Apiratikul P, Wang B, Guo S H and Richardson C J K 2014 *Opt. Express* **22** 7733
[21] Pressl B *et al* 2018 *Quantum Sci. Technol.* **3** 024002
[22] Günthner T, Pressl B, Laiho K, Geßler J, Höfling S, Kamp M, Schneider C and Weihs G 2015 *J. Opt.* **17** 125201
[23] Autebert C, Trapateau J, Orieux A, Lemaître A, Gomez-Carbonell C, Diamanti E, Zaquine I and Ducci S 2016 *Quantum Sci. Technol.* **1** 01LT02
[24] Kang D, Anirban A and Helmy A S 2016 *Opt. Express* **24** 15160
[25] Boitier F *et al* 2014 *Phys. Rev. Lett.* **112** 183901
[26] Bijlani B J, Abolghasem P and Helmy A S 2013 *Appl. Phys. Lett.* **103** 091103
[27] Vallés A, Hendrych M, Svozilík J, Machulka R, Abolghasem P, Kang D, Bijlani B J, Helmy A S and Torres J P 2013 *Opt. Express* **21** 10841
[28] Horn R T *et al* 2013 *Sci. Rep.* **3** 2314
[29] Kang D, Kim M, He H and Helmy A S 2015 *Phys. Rev.* A **92** 013821
[30] Schlager A, Pressl B, Laiho K, Suchomel H, Kamp M, Höfling S, Schneider C and Weihs G 2017 *Opt. Lett.* **42** 2102
[31] Machulka R, Lemr K, Haderka O, Lamperti M, Allevi A and Bondani M 2014 *J. Phys. B: At. Mol. Opt. Phys.* **47** 215501
[32] Bhar G C, Das S and Chatterjee U 1989 *Appl. Opt.* **28** 202
[33] Chen J, Pearlman A J, Ling A, Fan J and Migdall A 2009 *Opt. Express* **17** 6727
[34] Zhu E Y *et al* 2011 *Advanced Photonics* (Optical Society of America) paper SOWC3
[35] Takesue H and Inoue K 2005 *Opt. Express* **13** 7832
[36] Yuan Z, Kardynal B E, Stevenson R M, Shields A J, Lobo C J, Cooper K, Beattie N S, Ritchie D A and Pepper M 2002 *Science* **295** 102
[37] Stevenson R M, Young R J, Atkinson K C P, Ritchie D A and Shields A J 2006 *Nature* **439** 179
[38] Christ A, Brecht B, Mauerer W and Silberhorn C 2013 *New J. Phys.* **15** 053038
[39] Pavesi L and Guzzi M 1994 *J. Appl. Phys.* **75** 4779
[40] Laiho K, Pressl B, Schlager A, Suchomel H, Kamp M, Höfling S, Schneider C and Weihs G 2016 *Nanotechnology* **27** 434003
[41] Chen H, Laiho K, Pressl B, Schlager A, Suchomel H, Kamp M, Höfling S, Schneider C and Weihs G 2019 *J. Opt.* **21** 054001
[42] Chen H *et al* 2018 *APL Photonics* **3** 080804
[43] Kauten T, Keil R, Kaufmann T, Pressl B, Brukner Č and Weihs G 2017 *New J. Phys* **19** 033017
[44] Pearson B J and Jackson D P 2010 *Am. J. Phys.* **78** 471
[45] Schneeloch J, Knarr S H, Bogorin D F, Levangie M L, Tison C C, Frank R, Howland G A, Fanto M L and Alsing P M 2019 *J. Opt.* **21** 043501
[46] Silverstone J W *et al* 2014 *Nat. Photon.* **8** 104
[47] Faruque I I, Sinclair G F, Bonneau D, Ono T, Silberhorn C, Thompson M G and Rarity J G 2019 *Phys. Rev. Appl.* **12** 054029
[48] Klyshko D N 1980 *Sov. J. Quantum Electron.* **12** 1112
[49] Davidson F and Mandel L 1968 *J. Appl. Phys.* **39** 62
[50] Gross R and Marx A 2014 *Festkörperphysik* De Gruyter Studium (De Gruyter) (available at https://books.google.at/books?id=zSGCoAEACAAJ)
[51] Kim C C, Garland J W and Raccah P M 1993 *Phys. Rev.* B **47** 1876–88
[52] Gehrsitz S, Reinhart F, Gourgon C, Herres N, Vonlanthen A and Sigg H 2000 *J. Appl. Phys.* **87** 7825
[53] Adachi S 1993 *Properties of Aluminium Gallium Arsenide* vol 7, ed S Adachi (London: Inspec)